Precise Measurement of Suspension Force in Two-Axis Actively-Positioned Bearingless Motor for a Comparison to 3D-FEM Analysis

Hiroya Sugimoto* and Akira Chiba
Tokyo Institute of Technology
Tokyo, Japan

Abstract

Bearingless motors are required in centrifugal pumps, reaction wheels and artificial hearts for the applications in semiconductor manufacturing, space applications and medical devices, respectively. Two-axis actively regulated bearingless motors have the advantages of low cost and compactness. Only two degrees of freedom are actively regulated in the radial *x*-*y* directions. Thus it is known that tilting motion causes serious interference to the radial position regulation. The interference occurs when the following three positions are not exactly corresponding; (i) the center of gravity of the rotor, (ii) the application point of the suspension force, and (iii) the position of the displacement sensors. A discrepancy in these positions causes tilting and axial displacements, which results in a reduction of radial suspension force. In this paper, a 3D-FEM analysis of the radial suspension force is carried out taking into account the rotor tilting displacement. A precise measurement method of the static radial suspension force is proposed and tested. The experiment results indicate a good correspondence to the finite element analysis.

1 Introduction

Bearingless motors combine the functions of a magnetic bearing and a motor together within the same stator/rotor frame. They can generate torque as well as a magnetic suspension force on the rotor so that there is no contact between the stator and rotor. They do not need oil or grease lubrication and are free from contamination if sealed. It is anticipated that their main applications lie in the areas of semiconductor manufacturing, space travel, medical devices, as well as many others [1].

The literature reports on bearingless motors with one to five axes of active magnetic suspension. An active regulation of five degrees of freedom (5DOF) is employed in many bearingless or self-bearing motors [2-5] to acquire high output power or high reliability. However, if disturbance is not significant, then, magnetic suspension can be realized by only active two degrees of freedom (2DOF) regulation in radial directions [6-10]. The 2DOF bearingless motors are more compact and low cost.

In the 2DOF bearingless motors, the axial and tilting directions are passively positioned. Thus, flat disc shape is necessary to enhance the stiffness of the passive positioning. However, the authors have previously shown that the tilting rotor displacement has influence on the rotor positions detected by the displacement sensors [11]. In this case, the position sensors and the sensor target ring have been installed on lower side of the stator and the rotor. The interference occurs when the following three positions are not exactly corresponding; (i) the center of gravity of the rotor, (ii) the application point of the suspension force, and (iii) the position of the displacement sensors.

In this paper, a mathematical modeling of radial magnetic suspension system including the tilting rotor displacement is shown. When the axial position of the center of the lamination stack is not corresponding to the center of gravity of the rotor, the tilting torque and displacement are generated by the radial suspension force. Moreover, the axial position of the displacement sensors has influence to a feedback signal of the radial displacement. It is shown that the discrepancy in the axial positions cause measurement error. The measurement of the radial suspension force is carried out with additional balancing jig so that the tilting displacement is minimized. It is found that measured radial force in the experiment have a good correspondence to those in three-dimensional finite element method (3D-FEM) analysis.

*sugimoto@belm.ee.titech.ac.jp, 2-12-1 Ookayama, Meguro, Tokyo, Japan, +81-03-5734-2697

2 Rotor Static Modeling

2.1 Principle of Suspension Force Generation

Fig. 1 shows the structure of a multi-consequent-pole bearingless motor. The principle of radial suspension force generation is illustrated. The stator is circular with slots and teeth, although these are not illustrated for simplicity. The rotor is in a disc shape. It is a consequent-pole type. It has permanent magnets (PMs) magnetized in radial direction. The magnetization directions are identical in the radial direction since the rotor poles are alternated by PM and iron, so that there is one PM per one pole pair. The PMs are set into the rotor iron so that there are alternate iron poles. In the figures, the rotor has 20 PM poles and 20 iron poles, thus, totally 40 poles.

In consequent-pole bearingless motors, 2-pole magnetic field is required to generate suspension force. The flux generated by the PMs (hereafter referred as PM flux) goes through the stator and returns via the rotor iron pole. The flux suspension generated by the current in the 2-pole suspension coils N_y goes through the rotor via the iron poles because the permeance is higher than that of the PM pole. The superposition of the two fluxes produces the correct conditions to generate flux in the air-gap which is unbalanced, which, in turn, leads to a radial force. In the figure, the suspension force is generated in the y-axis negative direction. With a positive suspension current then positive force is generated. For x-axis force generation, another set of suspension windings N_x are wound in the stator in a spatial orthogonal direction. A vector sum of the x and y axis forces means the machine can generate suspension force in any radial direction. Even though the rotor rotates, radial suspension force is generated in the same direction by same suspension current. Therefore, consequent-pole type bearingless motors can generate the radial suspension force without depending on the rotor rotational angle. In reality, the two phase suspension winding is replaced by a three phase winding. Therefore the rotor can be actively positioned by a suspension force in any radial direction.

Fig. 2 shows the suspension and the motor winding structures of u-phase. The suspension winding consists of 3-phase and 2-pole with a toroidal structure. On the other hand, the motor winding consists of 3-phase and 40-pole with a fractional concentrated structure. The other phases, v- and w-phases, are offset by 120 mechanical degrees.

In Figs. 3 (a) and 3 (b) show the rotor tilting displacement. A restoring torque is generated by fringing fluxes between the rotor PMs and the stator core. Thus, the tilting directions are passively stable. The axial direction is also passively stable by the restoring force.

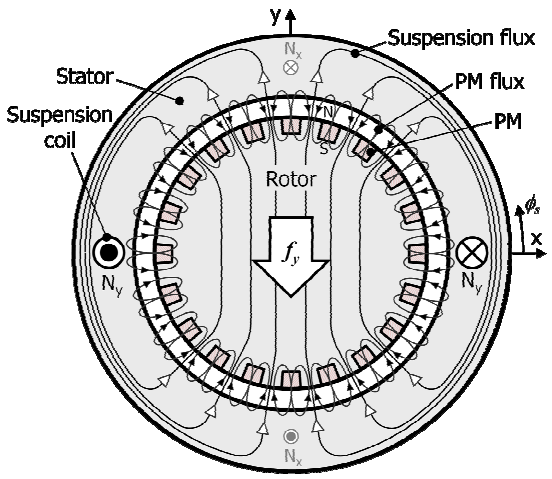

Fig. 1. Principle of radial suspension force generation.

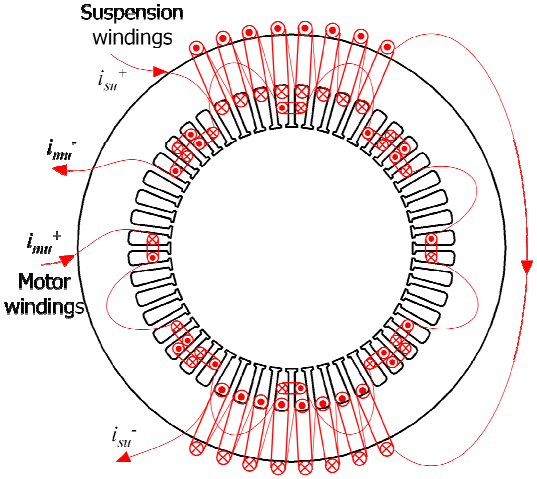

Fig. 2. Windings structure.

2.2 Static Force and Moment Equation

Fig. 3 (a) shows the y-z cross sectional view of misaligned rotor. On the right side of the rotor, a sensor target ring is constructed in tandem. The center of gravity of the rotor is located at distance of L_F from the center of the lamination stack. The displacement sensors are installed on the right side of the stator, so that these sensors are confronting to the target ring. The point G is the center of gravity of the rotor. The point S is the sensing position. The point F is the center of lamination stack. It is seen that the center of gravity of the rotor, the center of lamination

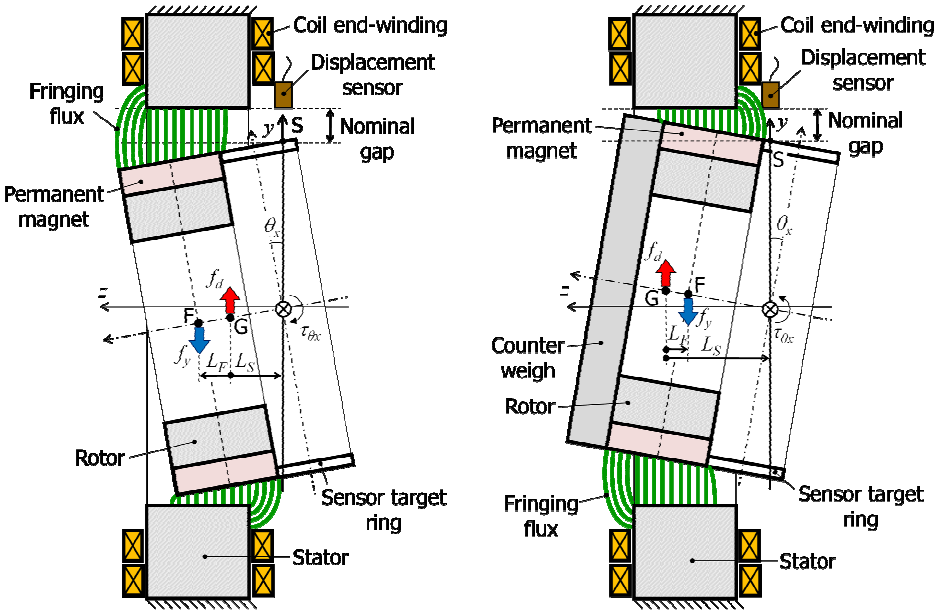

(a) $L_F > 0$ and $L_S < 0$. (b) $L_F < 0$ and $L_S < 0$.

Fig. 3. Restoring torque generation at the rotor tilting displacement.

stack and sensing position are different in the axial direction. The z-axis distances of points S and F from G are defined as L_S and L_F, respectively. Note that the signs of L_S and L_F are negative and positive, respectively in Fig. 3 (a).

Suppose that a radial disturbance force f_d is provided at the point G in the y-direction. The radial suspension force f_y is automatically generated by a negative feedback at the point F because the active radial position regulation is adapted. Therefore, the force equilibrium equation is given by

$$f_y = f_d - mg \tag{1}$$

where m is the rotor mass, g is gravity acceleration. Gravity is acting in the y-axis negative direction. Moreover, the tilting moment is generated around the point G with the force at the point F and point G. The moment rotates the rotor around x-axis so that the restoring torque is generated. The moment equilibrium equation around point G is given by

$$f_y L_F = k_t \theta_x \tag{2}$$

where k_t is the tilting stiffness, θ_x is the tilting angle around x-axis. The k_t is obtained experimentally from the rotor tilting inertia J and the natural angular frequency ω_θ as $J\omega_\theta^2$. The J is calculated by a 3D-CAD software (SolidWorks, Dassault Systems SolidWorks, Corp.). The ω_θ was measured by the experimental method in reference [12]. The J and k_t are shown in Table 2 in later section. The θ_x increases with an increase of the f_y or L_F. The tilting displacement around the point G causes the radial displacement of the point S in the y-axis positive direction. When an integral regulation is included in the radial suspension controller, the point S is maintained at the nominal position. Thus, the tilting displacement of the rotor results in the radial displacement in the y-axis negative direction. The radial displacement y_F of the point F is expressed by

$$y_F = L_S \theta_x = \frac{f_y L_F L_S}{k_t} \tag{3}$$

where $\tan\theta_x$ is approximated by θ_x. The y_F increases with an increase of θ_x and L_s.

Fig. 3 (b) shows y-z section when a cylindrical counter weight is attached at the left side of the rotor. In this case, the signs of the L_F and L_S are both in negative. The rotor tilting direction is in opposite to that in the Fig. 3 (a). The radial displacement of the points F and G are positive in the y-axis, although these are negative in Fig. 3 (a). Note that y_F is negative and positive in Figs. 3 (a) and 3 (b), respectively. The y_F causes radial force. Even though an external disturbance force is applied exactly at position G, the generated radial suspension force varies depending on the axial position of F. Thus the relation of radial force and current is influenced by the positioned the center of

gravity.

2.3 Radial Suspension Force Analysis with Rotor Tilting Displacement

Table 1 shows the θ_x and y_F variations when the L_F and L_S are 1 mm and -16.5 mm, respectively. These values are originated from an experimental setup as explained later. Substituting f_y, the θ_x and y_F are derived from the expression (2) and (3), respectively. A required suspension current is derived from magnetic field analyses. For example, a three-dimensional analysis model is constructed with at θ_x = 0.093 deg and y_F = -0.027 mm. Then the suspension currents are varied from 1 A to 1.3 A with a step of 0.1 A. The relation between the suspension currents and the radial suspension forces is plotted with linear approximation. From the approximated line, the suspension current that corresponds to the suspension force is found. The suspension current i_y is given by

$$i_y = \frac{f_y - b}{a} \tag{4}$$

where the constants a and b are the slope and intercept of the linearized expression.

Fig. 4 shows the obtained radial suspension force against the suspension current at the L_F = 1 mm and L_S = -16.5 mm. The plots indicate the radial force obtained by 3D-FEM with given inclination θ_x and displacement y_F in the rotor. The approximated lines are also drawn. The suspension currents for the radial suspension forces of 20 N, 40 N and 60 N are obtained to 0.37 A, 0.71 A and 1.05 A, respectively. Required suspension currents at various f_y, L_F and L_S are also calculated.

Fig. 5 shows the suspension force versus the current at various combinations of L_F and L_S. The current-force factor, that is the rate of change of f_y, is high as L_F is increased. According to the equation (3), the radial position of point F is displaced from the center with an increase of L_F. As seen from Fig. 3 (a), the direction of the radial displacement corresponds to that of the radial suspension force f_y. Therefore, the current-force factor is increased. On the other hand, in a case of Fig. 3 (b), the current-force factor is decreased because the direction of the radial displacement is opposite to that of radial suspension force.

The y_F is proportional to the product of the L_F and L_S. It is zero when the L_F is corresponding to zero. A precise measurement of the relation between the radial force and the current is performed because a magnetic attraction force due to the radial eccentricity is not generated.

Table 1. θ_x and y_F variation at L_F = 1mm, L_S = -16.5 mm.

f_y [N]	θ_x [deg]	y_F [mm]	a	b
0	0.000	0.000	0.000	0.000
20	0.031	-0.009	52.072	0.835
40	0.062	-0.018	53.177	2.199
60	0.093	-0.027	54.182	3.222

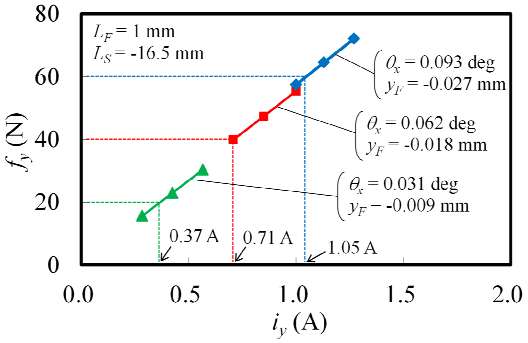

Fig. 4. Required suspension current.

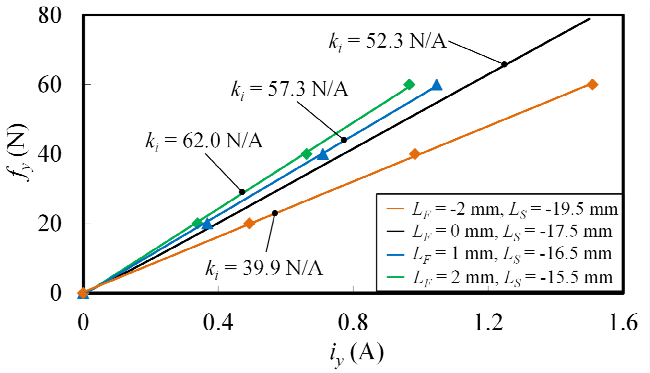

Fig. 5. Radial force and current at various L_F and L_S.

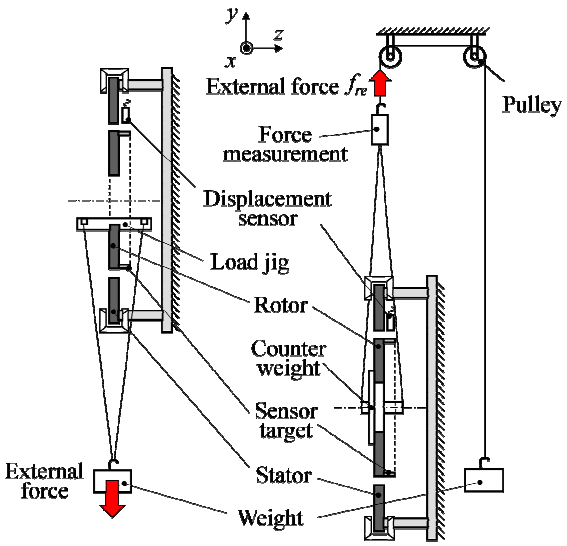

(a) Conventional method. (b) Proposed method.
Fig. 6. Experimental method of the radial suspension forces.

3 Experimental Method

Fig. 6 shows the experimental methods of the radial suspension forces. Fig. 6 (a) shows the conventional method. The gravity direction aligns with *y*-axis. A load jig is attached inside of the rotor. External forces are applied to the rotor in the *y*-axis negative direction by adding weight. In the conventional method, the measured current-force factor is high because the signs of the L_F and L_S are L_F = 2.05 mm and L_S = -15.45 mm, respectively. In addition, the suspension force less than the rotor weight cannot be applied.

Fig. 6 (b) shows the proposed method. A counter weight is attached to the rotor. The counter weight is designed so that the rotor center of gravity corresponds to the lamination center. The L_F is reduced from 2.05 mm to 0.01 mm. In addition, the external force is applied to the *y*-axis positive direction so that the measurements in the low suspension force region are possible. Force gauge (DS2-200N, IMADA, Co., Ltd., Japan) is used to measure the external force. The radial suspension force is given by

$$f_y = f_{re} - mg \tag{5}$$

where f_{re} is the reading of the force gauge. The three-phase suspension winding currents i_u, i_v and i_w are measured by a digital power meter (WT1600, Yokogawa, Electric Corp., Japan). The suspension current i_x and i_y are calculated by the transformation from three-phase to two-phase as

$$\begin{bmatrix} i_x \\ i_y \end{bmatrix} = \sqrt{\frac{2}{3}} \begin{bmatrix} 1 & -2/1 & -2/1 \\ 0 & \sqrt{3}/2 & -\sqrt{3}/2 \end{bmatrix} \begin{bmatrix} i_u \\ i_v \\ i_w \end{bmatrix} \tag{6}$$

The current-force factor in *y*-axis direction is given by

$$k_{iy} = \frac{f_y}{i_y} \tag{7}$$

However, an undesirable suspension force f_{xy} is generated in the *x*-direction due to interference force. The interference is evaluated as an angle error ϕ_e of the radial suspension force. In this paper, the angle error is defined as

$$\phi_e = tan^{-1}\left(\frac{f_{xy}}{f_y}\right) \tag{8}$$

The small angle error must be small enough to achieve a stable magnetic suspension. The consequent-pole bearingless motor need not have angular position sensors.

4 Experimental Results

Figs. 7 (a) and 7 (b) show the conventional and proposed rotors for precise measurement. In the proposed rotor, the rotor inner hole is filled by a counter weight. Table 2 shows the parameters of the proposed machine. The stator core diameter is 300 mm with a lamination stack length of 10 mm. The magnetic air-gap is 1 mm and the rotor diameter is 150 mm. The mass of the rotor, including a sensor target and a shaft which is mounted on the rotor, is 1.83 kg. The cores of the stator and rotor are made of silicon steel lamination. The PMs are made from NeFeB. The suspension controller consists of a microprocessor, two inverters and two sensor amplifiers. The rated capacity of the inverter is 100 V and 3 A.

Fig. 8 shows the measured suspension force in the y-axis direction with respect to the measured current in the proposed method. It also plots the relationship obtained by the 3D-FEM with $\theta_x = 0$ deg and $y_F = 0$ mm, when the rotor is centered. The rotor angular positions are set to 2.5° and 182.5° in mechanical angles because of cogging torque. At these mechanical angles, the electrical angles are identical to the electrical angle of 50°. The averages of the current-force factor are 50.8 N/A and 52.3 N/A in experiment and analysis, respectively.

Fig. 9 shows the current-force factor as a function of rotor rotational angle. The measurements were performed at the positions that were fixed by the cogging torque, i.e., 50°, 125°, 200°, 265° and 300° in the electrical angles. At the electrical zero angular position, a PM center faces to the x-axis direction. The averages of the current-force factors are 52.1 N/A and 52.8 N/A in the experiment and the 3D-FEM, respectively. The error between the measured and calculated values is found to be only 1.3 %.

Fig. 10 shows the mechanical angle errors of the radial suspension force. The maximum angle errors are 1.1 deg and 2.1 deg in the experiment and 3D-FEM, respectively. The maximum angle error is increased to 4.3 deg when the

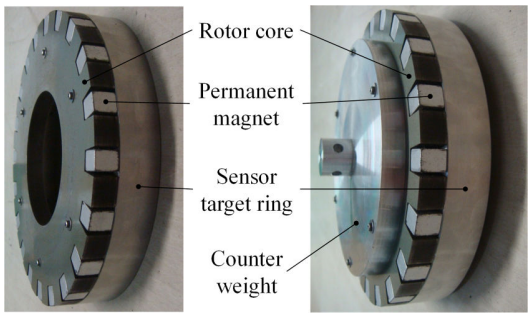

(a) Conventional. (b) Proposed.

Fig. 7. Rotors of the test machine.

Table 2. Machine parameters.

Plant		Value	Unit
Rotor mass	m	1.83	kg
Rotor moment of inercia	J	0.00275	kg·m^2
Rotor outer radius	r	75	mm
magnetic gap	l_g	1	mm
Stack length	L	10	mm
z coordinate of point F	L_F	0.01	mm
z coordinate of point S	L_S	-17.49	mm
Tilting stiffness	k_t	41.4	Nm/rad
Rotor			
Number of poles	p	40	
Permanent magnet material		Nd-Fe-B	
Windings			
Number of motor windins		70 turns / tooth	
Number of suspension windins		40 turns /slot	

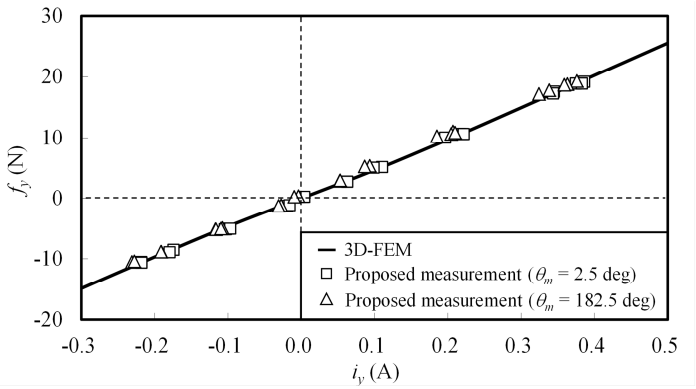

Fig. 8. Current versus radial suspension force.

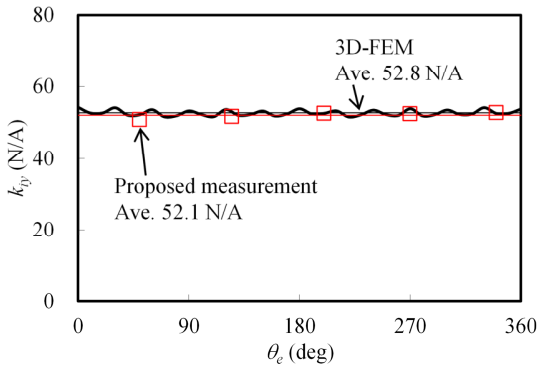

Fig. 9. Radial suspension force variation.

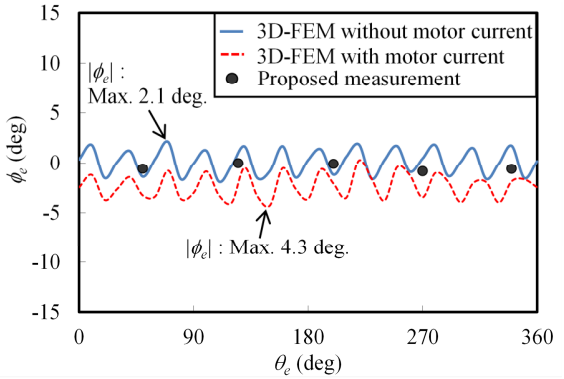

Fig. 10. Angle error of the radial suspension force.

rated motor current 1 A is provided in the motor winding. This angle error is small enough to realize stable magnetic suspension. In the motor acceleration test from 0 to 100 r/min, stable rotor levitation and rotation are successfully achieved.

5 Conclusion

In this paper, a static model of two-axis actively regulated bearingless motor including the tilting rotor displacement is presented. A 3D-FEM analysis with tilting motion and eccentric displacement was carried out. The current-force factors are varied due to the L_F and L_S, where L_F and L_S are the distances of force and sensor axial positions, respectively, from the center of gravity. Hence, the L_F and L_S have to be reduced in experiments.

In the proposed experimental method, the radial suspension force was measured. Then, a good correspondence is obtained. The averages of the current-force factors are 52.1 N/A and 52.8 N/A in the experiment and the 3D-FEM, respectively. The error between the measured and calculated values is found to be 1.3 %.

References

[1] A. Chiba, T. Fukao, O. Ichikawa, M. Oshima, M. Takemoto and D. G. Dorrell, "Magnetic Bearings and Bearingless Drives", Newnes Elsevier 2005 March 381pages ISBN 07506 5727 8 (2005)

[2] Z. Ren and L. S. Stephens : "Closed-Loop Performance of a Six Degree-of-Freedom Precision Magnetic Actuator", *IEEE/ASME Trans. Mechatronics*, Vol.10, No.6 pp-666-674 (2005)

[3] Tatsuya Ishikawa, Ken-ichi Matsuda, Ryo Kondo and Toru Masuzawa : "5-DOF Controlled Self-Bearing Motor", *Journal of System Design and Dynamics*, Vol.3, No.4 pp-483-493 (2009)

[4] M. Takemoto, S. Iwasaki, H. Miyazaki, A. Chiba and T. Fukao : "Experimental Evaluation of Magnetic suspension Characteristics in 5-axis Active Control Type Bearingless Motor without a Thrust Disk for Wide-gap Condition", *in Proc. Energy Convers. Congr. and Expo. (ECCE)*, pp. 2362-2367 (2009)

[5] J. Asama, M. Amada, N. Tanabe, N. Miyamoto, A. Chiba, S. Iwasaki, M. Takemoto, T. Fukao and M. A. Rahman : "Evaluation of a Bearingless PM Motor with wide magnetic gaps", *IEEE Trans. Energy Convrs.*, Vol.25, No.4 pp.957-964 (2010)

[6] Toru Masuzawa, Toshiyuki Kita and Yohji Okada, "An Ultradurable and Compact Rotary Blood Pump with a Magnetically Suspended Impeller in the Radial Direction", Artificial Organs, Vol.25, No.5 pp.395-399 (2001)

[7] P. Karutz, T. Nussbaumer, W. Gruber and J. W. Kolar : "Novel Magnetically Levitated Two-Level Motor", *IEEE/ASME Trans. Mechatronics*, Vol.13, No.6 pp. 658 – 668 (2008)

[8] W. Gruber and W. Amrhein : "Bearingless Segment Motor With Five Stator Elements—Design and Optimization", *IEEE Trans. Industry Applications*, Vol.45, No.4 pp.1301-1308 (2009)

[9] H. Sugimoto, K. Kamiya, R. Nakamura, J. Asama, A. Chiba and T. Fukao : "Design and Basic Characteristics of Multi-Consequent-Pole Bearingless Motor With Bi-Tooth Main Poles", *IEEE Trans. Magn*. Vol.45, No.6 pp.2791-2794 (2009)

[10] J. Asama, R. Kawata, T. Tamura, T. Oiwa and A. Chiba :"Reduction of force interference and performance improvement of a consequent-pole bearingless motor", *ELSEVIER Precision Engineering*, 36, pp.10-18 (2011)
[11] N. Watanabe, H. Sugimoto, A. Chiba, T. Fukao, "Basic Characteristic of the Multi-Consequent-pole Bearingless Motor," *in Proc. PCC Nagoya*, pp.1565-1570 (2007)
[12] J. Asama, T. Asami, T. Imakawa, A. Chiba, A. Nakajima and M. A. Rahman : "Effects of Permanent-Magnet Passive Magnetic Bearing on a Two-Axis Actively Regulated Low-Speed Bearingless Motor ", *IEEE Trans. Energy Conversion*. Vol.26, No.1 pp.46-54 (2011)